Green Chemistry

Cost and Energy Efficient Cyclic Separation of 5-hydroxymethyl Furfural from an Aqueous Solution

Journal:	*Green Chemistry*
Manuscript ID	GC-ART-03-2021-000841.R1
Article Type:	Paper
Date Submitted by the Author:	06-May-2021
Complete List of Authors:	Hsiao, Yung Wei; University of Delaware, Chemical & Biomolecular Engineering Anastasopoulou, Aikaterini; University of Delaware, Chemical & Biomolecular Engineering Ierapetritou, Marianthi; University of Delaware, Chemical & Biomolecular Engineering Vlachos, Dion; University of Delaware

Cost and Energy Efficient Cyclic Separation of 5-hydroxymethyl Furfural from an Aqueous Solution

Yung Wei Hsiao, Aikaterini Anastasopoulou, Marianthi Ierapetritou, and Dionisios G. Vlachos*
Department of Chemical and Biomolecular Engineering, University of Delaware, 150 Academy Street, Newark, Delaware 19716, United States
RAPID Manufacturing Institute, Delaware Energy Institute (DEI), University of Delaware, 221 Academy Street, Newark, Delaware 19716, United States

Abstract
The efficient separation of 5-hydroxymethyl furfural (HMF) – a platform chemical in biomass valorization – from the reactive aqueous mixture of sugars is key to improving its economic production. Here we demonstrate a cyclic fixed-bed process that selectively adsorbs HMF from the aqueous phase, purifies the solute, and enables its subsequent desorption in a suitable solvent for downstream applications. This intensified process bypasses the traditional energy-intensive recovery of HMF via vacuum distillation. The adsorption and desorption performances of a commercially available polymer-based spherical activated carbon (PBSAC) are quantified in batch and continuous systems. The effects of temperature (25 – 90 °C) and co-existence of other components from the fructose dehydration reaction (fructose, formic acid, and levulinic acid) on adsorption are evaluated. Model predictions based on parameters extracted from batch isotherms describe reasonably the continuous experimental breakthrough curve with suitable transport parameters. It is demonstrated that HMF can be selectively purified and recovered, and the adsorption column can be reused for at least seven cycles tested here. A simple analysis further showcases nearly tenfold cost and energy savings for HMF separation. The framework outlined here can be applied to other biomass solutes.

Keywords: HMF, Adsorption, Desorption, Continuous Operation, Process Intensification

* Corresponding Author: vlachos@udel.edu

Introduction

With the rapid increase in global population and energy demand, biomass has emerged as a renewable carbon resource that nets minimal greenhouse emissions and can be sourced globally with little geographical limitation. Lignocellulosic biomass, such as agricultural waste, forestry residues, and energy crops, can be catalytically converted into commodity chemicals derived from petroleum. By converting the carbohydrate fraction of lignocellulosic biomass into sugars, through enzymatic or chemical pathways, platform chemicals, such as furfural and 5-hydroxymethyl furfural (HMF), can be produced. These platform chemicals can be used to create direct replacements of crude-oil molecules or new chemicals and products. As an example, HMF can then be converted into commodity chemicals, such as 2,5-dimethylfuran (DMF), furan dicarboxylic acid (FDCA), and γ-valerolactone (GVL), which among others are useable as solvents, transportation fuels, polymers for packaging or textiles, or fuel additives.[1] With further advancements, the US can produce over a billion ton of inedible lignocellulosic biomass by the year 2030 to satisfy ~33% of the fuels and 25% of the domestic chemicals.[2,3]

The aqueous phase acid-catalyzed dehydration of C6 sugars, such as glucose and fructose, has been extensively studied to produce HMF over chromium chloride,[4] hydrochloric acid,[5,6] zeolites,[7,8] acid resins[9] among many catalysts. Fructose dehydration gives a higher reaction rate and selectivity than glucose. Yet, fructose conversion suffers from low selectivity due to subsequent side reactions, such as rehydration of HMF to levulinic acid (LA) and formic acid (FA), and degradation into polymers known as humins. Using dimethyl sulfoxide (DMSO), as a co-solvent[10,11] or a replacement solvent[12], ionic liquids,[10,13,14] and biphasic systems, e.g., water with 2-butanol or methyl isobutyl ketone (MIBK)[11,15] as extracting solvents, gives enhanced HMF yield and selectivity and fewer byproducts due to the enhanced stability of HMF in organic solvents. Several continuous biphasic systems[16–18] have also demonstrated high fructose conversion and HMF selectivity, and most importantly, improved productivity. Still, biphasic systems often experience a low partition coefficient (ratio of HMF in each solvent) of ~1, leading to the usage of a large amount of the organic solvent. While salts[19] or phenols[20] can also enhance HMF partition (i.e., from 44% to 87.5% of the total HMF), they are not ideal due to thze potential of plugging or toxicity, respectively, while a significant fraction of HMF remains in the aqueous phase. Extraction and purification of this highly reactive intermediate are foundational for downstream applications. The isolation of HMF from the aqueous phase or high boiling point solvents through low-temperature vacuum evaporation or distillation[11,21] is an energy-intensive process. Furthermore, substantial HMF carbonization can also occur at high temperatures.[21] These technical barriers are part of the challenges preventing the commercialization of HMF production.

Solid adsorbents offer an alternative for HMF separation and purification from the reacting liquid that can be more affordable and energy-efficient. Biorefineries have utilized solid adsorbents to separate various compounds, such as phenols, furans, and HMF, produced in trace amounts during the acidic hydrolysis of biomass, as they are toxic to the subsequent yeast fermentation process.[22,23] Several adsorbents, such as activated carbon,[24–27] polymer resins,[28–30] organo-metallic frameworks,[31] and zeolites,[32–34] have been studied for HMF removal in batch systems. Among these materials, commercial activated BP2000 carbon exhibits the best adsorption performance.[24–27] Through simulation, Swift et al.[27] and Dornath et al.[35] demonstrated the concept of reactive adsorption of HMF in batch using activated carbon BP2000, where the total HMF yield increased up to 20%. However, very few studies of these adsorbents have been undertaken under actual reaction compositions, i.e., in the presence of an acid catalyst, reactant fructose, and side products (FA and LA). Furthermore, little is known about the application of adsorbents in continuous

operation. Recovery of HMF has also rarely been demonstrated. Therefore, a thorough adsorption and desorption study in a continuous cyclic system is needed to bridge the gap between general adsorbent assessment and practical utilization.

Morphological characteristics, such as high surface area, high pore volume, and low degree of surface functionalization of the adsorbent, are linked to preferential HMF adsorption.[33,36] However, packing an adsorption column requires high mechanical strength materials; highly porous fine-powder materials used in batch systems cannot be fixated using filters or frits. Pressure-drop also deems nano-materials impractical. While pelletization can tune the particle size, it often leads to irreversible morphological or compositional changes to the carbon due to using a binder or high pressures. Commercial carbon black, known as Polymer-Based Spherical Activated Carbon (PBSAC), exhibits high adsorption capacity and mechanical strength that enables packing of a fixed-bed adsorption column. It is derived from polymer-precursors synthesized from a mixture of styrene precursors into ideal spherical shapes and subsequently carbonized and activated using steam or carbon dioxide. This synthetic procedure leads to a low degree of surface functionalization that makes it suitable for HMF adsorption.

In literature, batch and continuous systems have been studied separately. Batch adsorption isotherm provides rapid screening of the adsorbent equilibrium and solute adsorption capacity, while continuous systems are renowned for their productivity. The Langmuir, Freundlich, and Redlich-Peterson isotherms have commonly been used to quantify adsorption.[37] On the other hand, the Thomas model[38,39] has widely been used to fit continuous data as it provides an analytical solution. Even though extensive studies have been done in each operation mode, very few cases have connected the two into a coherent model. For example, the assumptions employed in the Thomas model – Langmuir kinetics for adsorption, negligible axial dispersion and diffusion resistance, and a plug flow – do not hold when the Freundlich or Redlich-Peterson isotherms describe the batch data. While in practice, the Thomas model has been used to fit data of any equilibrium type (e.g. sorption of phenol,[40,41] dye,[42] or heavy metals[43] onto biomass or activated carbon), it is empirical in nature and requires existing continuous breakthrough data. This gap renders many batch isotherm data secluded from performance prediction in an adsorber column. Furthermore, no desorption model has been demonstrated previously. A complete cyclic process model is needed for rapid prediction and system optimization.

In this study, we propose a two-stage temperature swing adsorption-desorption fixed-bed process using PBSAC to enable the rapid extraction of HMF from the aqueous stream. The adsorption performance of PBSAC is evaluated experimentally in batch and continuous systems as a function of temperature and in the presence of multicomponent mixtures from sugar dehydration. We employ a rapid high-performance liquid chromatography (HPLC) detection method for continuous breakthrough experimental data collection. A continuous flow model is formulated and implemented in MATLAB using the Parabolic and Elliptical Partial Differential Equation (PDEPE) solver. Breakthrough curves are predicted using parameters extracted from batch experiments with transport parameters fitted to experimental data. The importance of the axial dispersion coefficient is discussed and put in context to published correlations. The recovery of the adsorbed HMF is assessed using water and isopropyl alcohol as HMF-desorption solvents. The effect of temperature on the recovery rate and efficiency is quantified. We demonstrate the cyclic process for multiple cycles without material degradation. Finally, a simple cost and energy analysis demonstrates the potential of the separation framework outlined here as a low-energy alternative to vacuum distillation or as a foundational scheme to *transfer* HMF from the aqueous

phase into a suitable organic solvent for downstream processing, e.g., the hydrodeoxygenation of HMF into 2,5-dimethyl furan (DMF) over a Ru/C catalyst.[44,45]

Experimental

Materials

D-fructose (99%), 5-hydroxymethyl-furfural (98%), levulinic acid (98%), hydrochloric acid (37%), and sodium chloride (99%) were purchased from Sigma-Aldrich. Potassium chloride (97%), formic acid (88%), and 2-propanol (≥99.5%) were purchased from Fisher Scientific. Polymer-based spherical activated carbon sample (PBSAC ID# 100043 was supplied by Blücher GmbH (Erkrath, Germany). All chemicals were used as received. Solutions were prepared using deionized water (Milli-Q, 18MΩ).

Adsorbent Characterization

Two material characteristics influencing the capacity and selectivity of the adsorbents are texture and surface functional groups. The textural properties of the porous material are obtained from nitrogen gas sorption at -196 °C using the Micromertics ASAP 2020 Brunauer Emmett Teller (BET) Analyzer. X-ray photoelectron spectroscopy (XPS, Thermo Fisher K-Alpha$^+$) was used to analyze the surface elemental composition of the adsorbent, where the samples were evenly coated onto a layer of carbon tape. Activated carbon sample, BP2000 (Cabot Corporation) – a carbon sample that has demonstrated high HMF adsorption in the literature[25,27,35,46] yet cannot be sufficiently pelletized for fixed-bed application – was analyzed on the XPS as a point of reference to minimize noise from the carbon tape.

Batch Adsorption Isotherms

The adsorption properties of PBSAC were assessed with batch experiments. 35 mg of PBSAC and 4 mL of solutions with solute concentrations from 1.25 to 20 mg/mL were combined in a 10 mL septum-sealed vial. Solutions for competitive adsorption were made with equal molar concentrations of fructose and HMF to emulate real fructose dehydration conditions. The yields of side products are typically lower than that of HMF; thus, the concentrations of FA and LA were taken as half of fructose.

The mixture was stirred on a heating plate for 4 hours at 25, 55, 90, and 120 °C. Samples were drawn from the vials after 4 hr using 22-gauge needles and 0.2 μm syringe filters. Both the needle and the filter were heated inside an oven to prevent the liquid from cooling down during the withdrawal process and alter the equilibrium. The experimental time for FA adsorption was shortened to 30 min to avoid deleterious effects of FA at elevated temperatures reported previously.[28,47,48] A luer lock valve (Sigma Aldrich) was used to entrap the heated liquid inside the syringe, where the sample was cooled down before transferred into an HPLC vial for quantification (Water Alliance Instruments HPLC 2695). The adsorption loading was calculated using Eq. 1. Experimental data was fitted using the Redlich-Peterson and Freundlich isotherms (Eq. 2). The isotherm parameters were extracted using the nonlinear fitting *cftool* interface in *MATLAB 2019b*. Here, q_{eq} is the equilibrium adsorbate loading on the adsorbent [mol_{HMF}/g_{carbon}], V is volume of the solution [mL], and C_0 and C_{eq} are the initial and equilibrium HMF concentrations in the liquid phase [M], respectively. K_{RP} is the Redlich-Peterson isotherm equilibrium constant [(L/g_{carbon})], b_{RP} is a constant related to the free energy of adsorption [$(L/mol)^n$], and n_{RP} is an empirical exponent between 0 and 1. The ratio K_{RP}/b_{RP} is indicative of the maximum adsorption capacity despite the unit mismatch. At the limit of $n_{RP}\rightarrow 1$, the equation reduces to the Langmuir isotherm.

Similarly, K_F is the Freundlich isotherm equilibrium constant [$(L/g_{carbon})^{1/n}$] and $1/n$ is a constant between 0 and 1. The quaternary competitive adsorption was then estimated using the Ideal Adsorption Solution Theory (IAST) and the estimated single component isotherms.[49,50]

$$q_{eq} = \frac{V(C_0 - C_{eq})}{m_{ads}} \quad (1)$$

$$q_{eq,RP} = \frac{K_{RP}C_{eq}}{1 + b_{RP}C_{eq}^{n_{RP}}}, \qquad q_{eq,\ F} = K_F C_{eq}^{n_F} \quad (2)$$

Fixed-bed Setup

Polyether ether ketone (PEEK) tubing (IDEX Health & Science) with OD = 1/8" and ID = 0.093" was used as the micro-fixed bed column. Carbon adsorbent was trapped inside the column using PEEK (2 μm) filters (IDEX Health & Science). Glass wool (Sigma Aldrich) was used on both ends of the column to create a thin layer (~1 mm) of shield between the adsorbent and the ends of the column and ensure packing tightness. The adsorbent was poured into the column using a small funnel. Then, the packed column was positioned vertically where 10 mL min^{-1} of deionized water was pumped through the column for >15 min to enable a tighter packing of the adsorbent using the gravitational force. Additional glass wool was added when necessary. Control columns were packed with glass beads of similar particle diameter (Sigma Aldrich, Acid-Washed, d_p =150-212 μm) to assess the entire system's residence time for the solute to travel down until the sample collection exit.

The void fraction was estimated using the water weight difference between a freshly packed column of wet particles and a column filled with water. The packing effectiveness was further assessed using a non-adsorbing ionic salt.[51–53]A 10 μL injection of 0.2 M sodium chloride solution was sampled using HPLC, where the fluid connection was redirected to enter the fixed-bed column. The salt tracer was carried by the flow media (DI and degassed water) into the packed column that was connected downstream. Flowrates between 0.3 and 1.1 mL min^{-1} were used to examine the residence time distribution and ensure the lack of column channeling. The salt tracer signal passed through the fixed bed column was detected using a refractive index detector (Waters RI 2414). The asymmetry factor was calculated as the ratio of the rear to front tracer half-peak width at 1/10 of the peak height.[54] Channeling was negligible. Additional information and calculations are in the Supplementary Information (SI) and Figure S1.

Continuous Setup and Adsorption Cycle

Three Teledyne LS Class High-Performance Isocratic Pumps (LS005PFT3A) with perfluoro alkoxy (PFA) and PEEK fluid paths were used to pump the liquid feeds. Fluid connections to the fixed bed column were made using either 1/8" to 1/16" PEEK reducing unions or 1/16" connecting unions, both supplied by Valco Instruments. A 1/16" PEEK 4-way manifold with 0.55 mm bore (Restek Corporation) was used to bundle all solvents and direct them to the column: the DI water stream and the adsorbate solution stream during Stage 1 (adsorption cycle) and desorbing solvent stream in Stage 2 (desorption cycle). This configuration allows rapid heating of the solvent without compromising the integrity of adsorbate with the acidified water. A manual shut-off valve was placed in front of the 100 psi check valve, where an artificial pressure built up could quickly purge and equilibrate the adsorbate line between the pressure regulator and the manifold when the valve was opened. In preliminary experiments, a 250 psi pressure difference could quickly equilibrate

the concentration within 3 min without ever overshooting the expected concentration (Figure S5). Three check valves (IDEX Health & Science) were placed before the cross of each stream to prevent backflow when the flow was stagnant and the experiment was in a different "stage." Teflon tape was used to seal the connections and prevent leaks created upon heating expansion and contraction cycles on the plastic lines. A 100 psi back pressure regulator (IDEX Health & Science) was used to condense the reacting mixture in the liquid phase at high temperatures. The entire experimental setup is shown in Scheme 1.

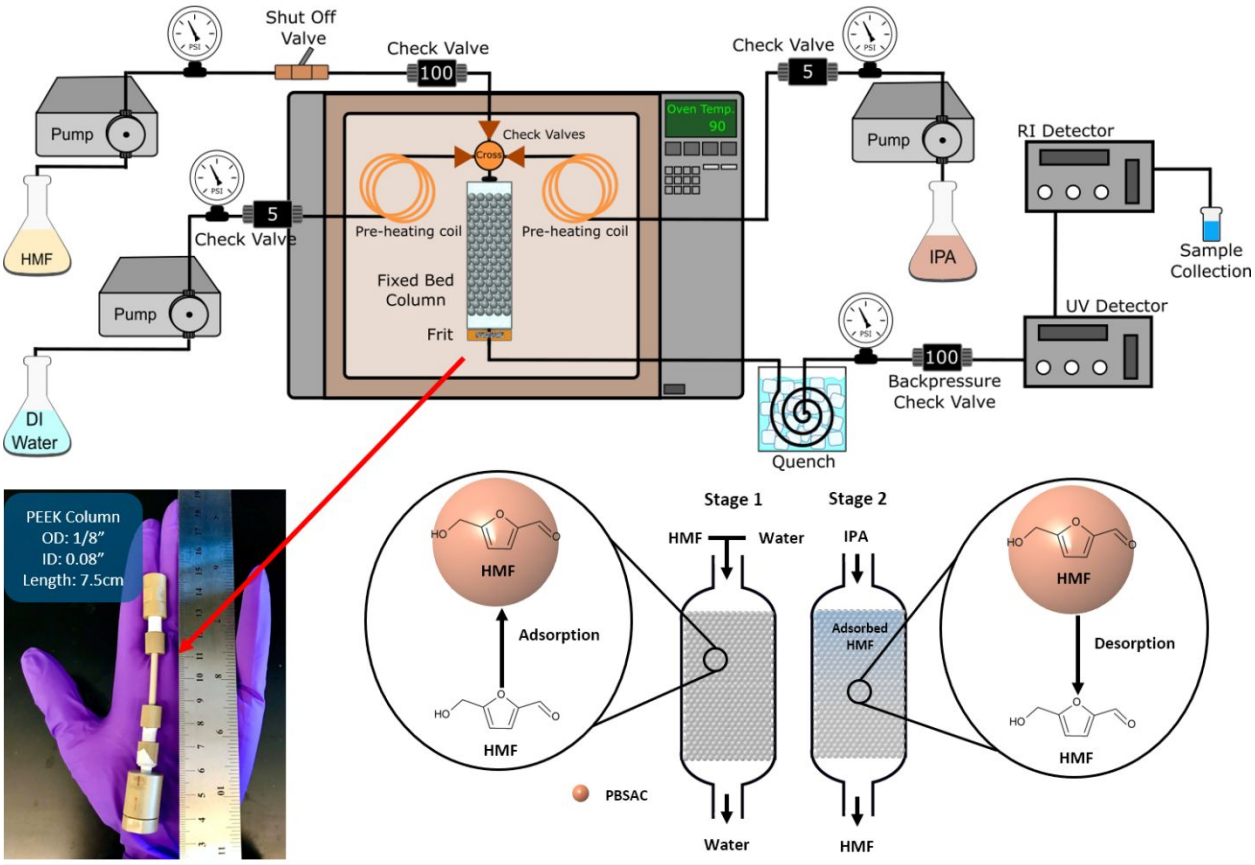

Scheme 1: *Overview of the continuous micro-fixed bed setup and adsorption/desorption stages.*

As shown in Scheme 1, two HPLC pumps deliver a stream of 12.5 wt% aqueous solution of the adsorbate and a stream of deionized water at a total flow rate of 1.1 mL min^{-1}. The water feed can be preheated to a temperature of interest (e.g., 25, 55, and 90 °C) inside a gas chromatograph (GC) oven. The solution with the adsorbate species at room temperature merges at the 4-way manifold with the hot stream at a ratio of 1:10, respectively. The large volume difference prevents the autocatalytic degradation of the adsorbates, especially fructose, in acidified water at higher temperatures. It ensures isothermal conditions where the temperature difference between the inlet and exit of the column was ~0.1 °C (Figure S4). The product liquid was filtered downstream using an in-line filter assembly (0.5 μm). The exit stream was routed to a refractive index detector (Waters RI 2414) and a UV/Visible detector (Waters 2998 PDA Detector) connected in-line for rapid detection of the asorbate breakthrough. Fructose was detected on the RI detector, while HMF, FA, and LA were individually detected on the UV detector at 355 nm, 211 nm, and 254 nm wavelengths, respectively. Products were collected at the outlet and subsequently quantified by

HPLC. Continuous adsorption experiments of individual adsorbate species were conducted at 25, 55, and 90 °C, while competitive adsorption was undertaken only at 25 °C.

Desorption Cycle

Upon bed saturation, HMF needs to be recovered using a solvent. Two obvious solvent traits are (1) its high HMF affinity and (2) its suitability for downstream processing. Alcohols recover 90-100% of HMF using multiple overnight washings in batch.[27,28] Secondary alcohols, such as isopropyl alcohol (IPA), can serve as hydrogen donors and solvents for hydrodeoxygenation.[44,45,55] With these traits and knowledge in mind, IPA is chosen here as a desorption solvent for proof-of-concept. For increased productivity, recovery is demonstrated in the continuous system.

The column was first saturated with HMF. After that, the HMF/DI water stream was immediately switched off, and the pump of the desorption solvent was turned on. HMF was desorbed from the saturated column using either water (a reference solvent) or IPA at 25 or 90 °C. The adsorbed and desorbed amounts were calculated from the area between the breakthrough curve and the $C/C_0 = 1$ line, and the area below the breakthrough curve with the zero line, respectively. The recovery efficiency [~] was calculated using Eq. 3, where W_a is the amount of HMF adsorbed in Stage 1 [mg] and W_d is the amount desorbed [mg] from the adsorbent, over a set time of an experiment (45 min). Subsequent adsorption cycles followed immediately after the completion of each desorption cycle.

$$Recovery = \frac{W_a}{W_d} * 100\% \quad (3)$$

Fixed-bed Model and Simulation

A simple mass balance model[56] describes the isothermal adsorption and desorption in the column. Eq. 4 is the mass balance, where v is the interstitial velocity [m/s], ε is the bed void fraction [~], and D_z is the axial dispersion coefficient [m^2/s]. The adsorption rate $\frac{\partial q}{\partial t}$ is controlled by the linear driving force between the equilibrium adsorbate concentration on the outer particle surface q (calculated based on the bulk liquid concentration) and the average adsorbate concentration q_{eq} in the particle, multiplied by the lumped mass transfer coefficient k_{res}.[57–59] In this case, we assumed that the diffusion in the spherical adsorbent particles is governed by external film mass transfer resistance. The Schmidt number was estimated using the diffusion coefficients D_f from the literature[60–62] and further used to calculate the Sherwood number and the external mass transfer coefficients for each component using the empirical correlation presented by Gabitto *et al*.[63] The estimated k_{res} is consistent with the finding that the rate of adsorption is fast (Figure S6). In the case of fructose, which exhibits a relatively sluggish experimental breakthrough curve, the local equilibrium theory (using Eq. 6 and the isotherm) was employed assuming infinitely fast mass transfer rates and negligible dispersion.[64] The adsorbate loading at equilibrium q_{eq} is calculated using the Freundlich isotherm (for HMF, FA, and LA) due to its mathematical simplicity and numerical stability, and the Langmuir isotherm for fructose. Initial and boundary conditions are shown in Eqs. 7 and 8, respectively. Eq. 4 was nondimensionalized using variables outlined in Eq. 9 into Eq. 10 & 11, and solved using PDEPE. The dimensionless Péclet number ($Pé$) were obtained from fitting experimental data and compared to literature correlations.[65–67] The desorption model uses the same mass balance equation with revised boundary and initial conditions (Eq. 12). Again,

the local equilibrium theorem was employed given the fast desorption rate of HMF into IPA observed in the experiments. Model predictions were compared to experimental breakthrough data, and the sum of the squares of the error (Eq. 13) was calculated, where C_{model} and C_{exp} are the predicted and experimentally determined effluent concentrations normalized by the influx concentration C_0, and N is the total number of data points.

$$\frac{\partial C}{\partial t} = D_z\frac{\partial^2 C}{\partial z^2} - v\frac{\partial C}{\partial z} - \frac{(1-\varepsilon)}{\varepsilon}\rho_c\frac{\partial q}{\partial t} \quad (4)$$

$$\frac{\partial q}{\partial t} = k_{res}(C - C_{eq}) = \frac{3k_f}{r_p}(C - C_{eq}) \quad (5)$$

$$\frac{\partial q}{\partial t} = \frac{\partial q \partial C}{\partial C \partial t} \quad (6)$$

$$IC\text{: } C|_{t=0} = 0 \ \ \& \ \ q|_{t=0} = 0 \ for \ z \geq 0 \quad (7)$$

$$BC\text{: } C|_{z=0} = C_0 \ \ \& \ \ \frac{\partial C}{\partial z}|_{z=L} = 0 \ \ \ for \ t > \ 0 \quad (8)$$

$$\tau = \frac{tv}{L}, \zeta = \frac{z}{L}, C^* = \frac{C}{C_0}, Pé = \frac{vL}{D_{ax}}, q^* = \frac{q}{q_0}, \psi = \frac{(1-\varepsilon)\rho_p q_0}{\varepsilon C_0} \quad (9)$$

$$\frac{\partial C^*}{\partial \tau} = \frac{1}{Pé}\frac{\partial^2 C^*}{\partial \zeta^2} - \frac{\partial C^*}{\partial \zeta} - \psi\frac{\partial q^*}{\partial \tau}$$

$$\frac{\partial q^*}{\partial \tau} = \frac{k_{res}L}{v}\left(C^* - {C_{eq}}^*\right) \quad or \quad \frac{\partial q^*}{\partial \tau} = \frac{\partial q^* \partial C^*}{\partial C^* \partial \tau} \quad (10)$$

$$\text{IC: } C^*|_{\tau=0} = 0 \ \ \& \ \ q^*|_{\tau=0} = 0 \ for \ \zeta \geq 0$$

$$\text{BC: } C^*|_{\zeta=0} = 1 \ \& \ \frac{\partial C^*}{\partial \zeta}|_{\zeta=1} = 0 \ \ \ for \ \tau > \ 0$$

$$q^* = \frac{K_f}{q_o}(C_{eq}^* C_o)^n \quad or \quad q^* = \frac{1 \ K_L b_L C_{eq}^* C_o}{q_o 1 + b_L C_{eq}^* C_o} \quad (11)$$

$$\text{IC: } C^*|_{\tau=0} = 1 \ \ \& \ \ q^*|_{\tau=0} = 1 \ for \ \zeta \geq 0 \quad (12)$$

$$\text{BC: } C^*|_{\zeta=0} = 0 \ \& \ \frac{\partial C^*}{\partial \zeta}|_{\zeta=1} = 0 \ \ \ for \ \tau > \ 0$$

$$SSE = \frac{\sum[(C_{model} - C_{exp})/C_0]^2}{N} \quad (13)$$

Both the adsorption and desorption models are subjected to the following assumptions: (a) Experiments were carried out at isothermal conditions, (b) the particle density and size are homogeneous, (c) the velocity field in the bed is uniform, and (d) the physical properties of the solvent remain constant.

Results and Discussion

Materials Characterization

The textural properties of PBSAC were obtained using low-temperature nitrogen adsorption-desorption isotherms (Figure S1a), and the pore size distribution was determined from the Barrett-Joyner-Halenda (BJH) adsorption (Figure S1b). The PBSAC isotherm resembles a mix of Type I and IV isotherms. The fairly horizontal plateau is distinctive of Type I isotherm, whereas the rounded knee and the hysteretic loop are characteristic of condensation in mesopores in Type IV isotherms. This result indicates that PBSAC possesses both micropores and mesopores, with the majority of pores at 1.7 nm and a tailing fraction of pores > 15 nm. The average pore size of PBSAC is 3.3 nm. The surface area of PBSAC estimated via BET is 1080 m^2 g^{-1}, which is comparable with most commercial activated carbon sorbents (Table S1).

To elucidate the relationship between the oxygen content and functional groups with sorbent performance, both PBSAC and BP2000 were analyzed using XPS (Figure S2). Comparison of the two sorbents indicates a twofold lower total oxygen on the surface of PBSAC. While the C 1s scan shows subtle fractions of carboxylate (O-C=O, 288.7 eV), carbonyl (C=O, 287.4 eV), and C-O (285-286 eV) functional groups on PBSAC, the carboxylate and C-O peaks on the BP2000 surface are prominent.[68] The functional groups in BP2000 are consistent with those found by Yoo *et al.*[25] The overall oxygen content on the surface of PBSAC is low (4.1%) and comparable to that (5%) reported by Böhringer *et al.*[36] The textual properties of PBSAC are summarized in Table 1 and compared with those of other literature sorbents in Table S1.

Table 1: Textual properties of PBSAC.

Parameter	**Value**
Bulk Density [g/cm^3]	0.517
Surface Area [m^2/g]	1080
Pore Volume [cm^3/g]	0.899 (total) 0.499 (micro) 0.182 (meso)
Adsorbent Particle Diameter [μm]	192.5
Average Pore Width [nm]	3.31
Particle Porosity [~]	0.317
Elemental Analysis (C:O ratio)	95.8:4.1

Batch Adsorption

The adsorption performance of PBSAC was tested in batch with BP2000 as a reference adsorbent. The adsorption loading vs. time over PBSAC and BP2000 is shown in Figure S6. The two profiles are similar, and equilibrium is achieved in <5 min over both BP2000 and PBSAC. This short equilibration time is favorable for fixed-bed adsorption. The HMF diffusion coefficient is assumed to be constant due to the similar meso-/micro-pore size distributions of BP2000 and PBSAC. However, the rapid adsorption made it impossible to determine adsorption kinetics. Thus, it is assumed that adsorption is not rate-limiting in either the batch or the continuous system.

The batch adsorption isotherms of single components on PBSAC are shown in Figure 1. PBSAC has the highest adsorption loading for HMF, followed by LA, FA, and fructose, with HMF being the most hydrophobic component and fructose the most hydrophilic. As Yoo *et al.*[25] demonstrated, the oxygen functional groups make the surfaces more polar and hydrophilic, leading to a decreased HMF adsorption loading. Since PBSAC is more hydrophobic than BP2000 (a C:O ratio of 90.5 : 9.5), it is not surprising that PBSAC has a slightly higher HMF adsorption capacity than BP2000[27,35] despite its smaller surface area[69] (1080 m^2/g vs. 1374 m^2/g) and similar micropore

volume[69] (0.499 cm^3/g vs. 0.46 cm^3/g). Consistent with prior batch experiments on BP2000, our data indicates that the sorbent's hydrophobicity is essential in the selective adsorption of HMF.

The Redlich-Peterson and Freundlich models adequately describe the experimental data (see regression coefficients in Table S2). Using the van't Hoff relationship, $\Delta H = R\frac{\partial\, lnK}{\partial\, 1/T}$, the heat of adsorption was calculated from the equilibrium constant K of the Redlich-Peterson isotherm and is shown in Table 2. The estimated heat of adsorption for HMF of 47.4 kJ/mol is close to the 41 kJ/mol reported by Swift *et al.*[27] on BP2000. Since adsorption is exothermic, the loading decreases with increasing temperature. On the other hand, while the heat of adsorption cannot be estimated using the Freundlich model because it does not collapse into Henry's law at the low concentration limit, its two-parameter simplicity makes it suitable for modeling. Since both isotherm models describe experimental data equally well, the continuous flow system (see below) was modeled using the Freundlich isotherm due to its better numerical stability.

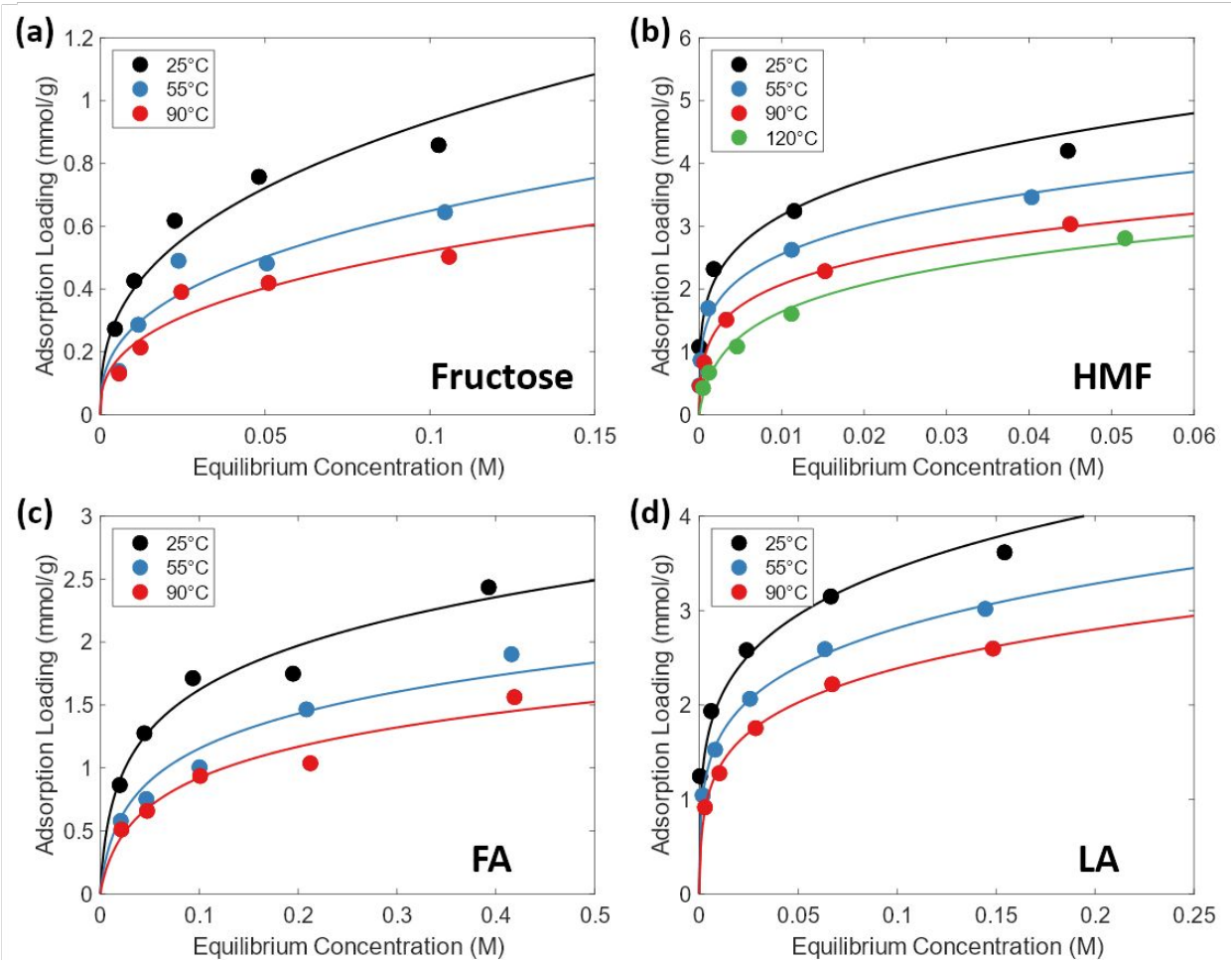

*Figure 1: Experimental adsorption isotherms (points) and isotherm fits (lines) of **(a)** fructose (Freundlich), **(b)** HMF (Redlich-Peterson), **(c)** formic acid (FA) (Redlich-Peterson), and **(d)** levulinic acid (LA) (Redlich-Peterson) on PBSAC at 25 °C (black), 55 °C (blue), 90 °C (red), and 120 °C (green, HMF only). The isotherm parameters are given in Table 2.*

Table 2: Fitted Redlich-Peterson adsorption isotherm parameters for single components. K and b are fitted to the Arrhenius form of $P = P_0 \exp(\Delta H/RT)$. The bolded ΔH values are the heat of adsorption for each species calculated using the adsorption equilibrium constant. Additional fitted parameter values are shown in Table S1.

Adsorbate	Exponent (n)		Pre-exponential (P_0)	ΔH (kJ/mol)	R^2
Fructose	0.37	K L/g_{carbon}	5.30E-04	**12.6**	0.9955
		b $(L/mol)^n$	6.85E+00	6.10	0.9495
HMF	0.77	K L/g_{carbon}	9.05E-07	**47.4**	0.9208
		b $(L/mol)^n$	7.57E-04	43.2	0.9110
FA	0.78	K L/g_{carbon}	2.05E-04	**16.5**	0.9962
		b $(L/mol)^n$	8.55E-01	10.3	0.9927
LA	0.78	K L/g_{carbon}	7.95E-04	**23.4**	0.9426
		b $(L/mol)^n$	7.34E-01	19.1	0.9717

While adsorption loading of single components is an important metric, selective adsorption of HMF from a multicomponent solution is essential in practice where multiple species are present. Competitive adsorption of four species involved in the fructose dehydration was studied in batch. Comparison of Figure 1 and Figure 2a shows that multicomponent mixtures lead to reduced uptake of each species. However, the total loading remains relatively constant, which points to competitive adsorption. Compared to the single component, the uptake of fructose, LA, and FA all drop by more than 80% in the presence of HMF, while the decrease in HMF uptake is less than 25%. A similar reduction in the adsorption loading of LA by HMF has also been observed by Detoni et al. using a nonpolar hyper-cross-linked polymer as the adsorbent.[28] This preferential selectivity towards HMF is further visualized using the separation factors α. Separation factors for each species are calculated using Eq. 14, where x_i and y_i are the molar compositions of component i in the effluent and feed streams, respectively, divided by the sum of the residual three components.[46,70] This is a modified form from its original binary mixture application. Calculation using the adsorption loading q_i yields the same result.

The separation factor as a function of solution concentration is shown in Figure 2b. Competitive adsorption initiates when the adsorbent is near saturation. As the sorbent becomes more utilized, HMF is preferentially adsorbed over weakly adsorbed solutes. The selective adsorption of HMF is at maximum (5.44) when the solution concentrations are the highest at 25 °C. The separation factors for fructose, HMF, FA, and LA are 0.01, 5.44, 0.05, and 0.10, respectively. Even though LA is the main competitor of HMF, we envision that in reactive adsorption, HMF would decrease the LA concentration in solution because LA forms solely from the rehydration of HMF, whose concentration in solution would be less.[4,71] On the other hand, while FA is generated from both fructose and HMF,[4] it adsorbs weakly and does not impact HMF adsorption. Each species' separation factor is weakly temperature-dependent, although the total loading decreases slightly with increasing temperature as expected for an exothermic process.

Complete data is given in Table S3. The high HMF adsorption capacity and selectivity of PBSAC renders it a promising adsorbent for reactive separation or separation studied here.

$$\alpha = \frac{x_i}{\sum_{j \neq i} x_j} \Big/ \frac{y_i}{\sum_{j \neq i} y_j} = \frac{q_i}{\sum_{j \neq i}^{m} q_j} \quad (14)$$

The IAST model is assessed in Figure 2a. The calculations are detailed in the SI; the model was validated using the literature's binary adsorption data.[28] As demonstrated previously, both the Freundlich and Redlich-Peterson isotherms describe the batch data well. While the Freundlich model reduces calculation complexity, the Redlich-Peterson model improves accuracy. Predictions in Figure 2a use the Freundlich model for fructose and the Redlich-Peterson model for HMF, FA, and LA (Table S2). This hybrid modeling leverages either the higher accuracy or the numerical stability of each isotherm. Discrepancies in the predictions may result from the solutes' nonideal interactions and the sensitive calculation of the spreading pressure. It is no surprise that very few works exit using the IAST model for 4-component predictions,[27] where the IAST accuracy decreases with increasing the number of compounds. Regardless, IAST is still a semiquantitative screening tool that describes the experimental data reasonably and could be used in future work for a more detailed design.

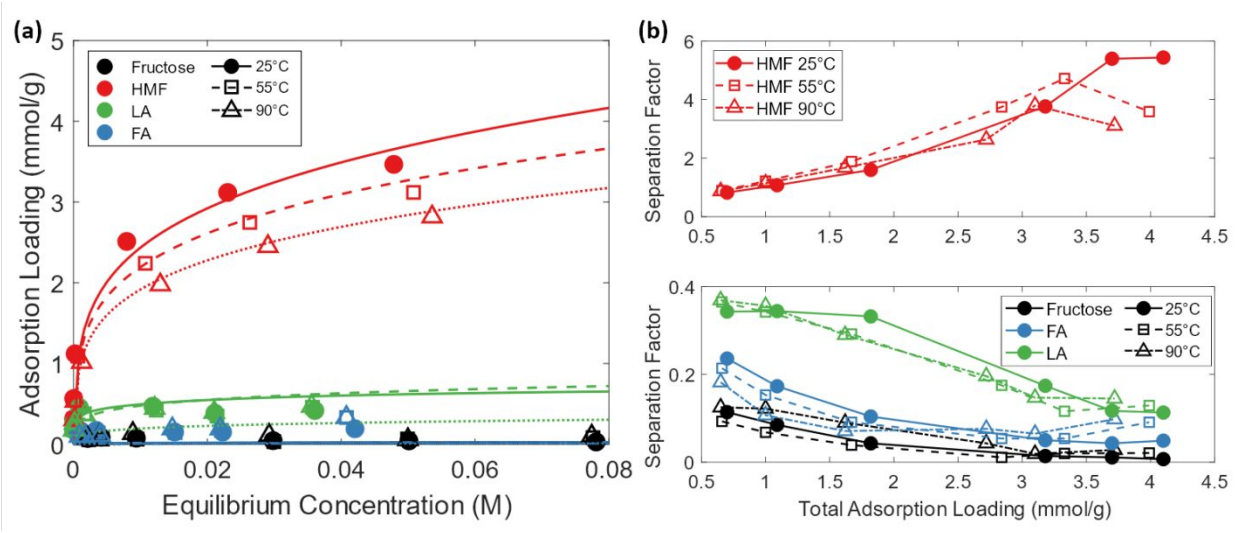

Figure 2: ***(a)*** *Competitive adsorption isotherms starting with equal-molar concentrations of fructose (black) and HMF (red) and half concentrations of FA (blue) and LA (green), at 25 °C (circles), 55 °C (squares), and 90 °C (upside-down triangles). Points are experimental data, and lines are the best-predictions calculated using the IAST model and parameters from Table 2.* ***(b)*** *Separation factor of each species vs. total adsorption loading. The total adsorption loading is the sum of four species loading and decreases slightly with increasing temperature as expected for an exothermic process.*

Fixed-bed Adsorption Performance

The average porosity of five different packed columns was 0.35; periodic inspections found this value to be reproducible. The column pressure drop was determined using the built-in pressure sensor of the HPLC pump. The parameters and operating conditions, summarized in Table 3, are later used for simulations.

Table 3: The operating conditions of the fixed-bed and parameters used for simulation of the breakthrough curves.

Parameter	**Value**
Column OD [inch]	1/8
Column ID [inch]	0.093
Column Length [cm]	10
Bed Void Fraction	0.35 ± 0.015
Flowrate [mL/min]	1.1
Column Pressure Drop (psi)	4-6
Initial Concentration [mg/mL]	1.25
Diffusion Coefficient, D_f [m^2/s]	$D_{f(HMF)}$=1.2 x 10^{-9} [60] $D_{f(LA)}$=1.2 x 10^{-9} * $D_{f(FA)}$=1.4 x 10^{-9} [61] $D_{f(Fru)}$=6.9 x10^{-10} [62]
Re	0.896

*Assumed to be the same as $D_{f(HMF)}$ given the lack of a literature value.

The adsorption fixed-bed performance is characterized by its breakthrough curve that describes the adsorbate-effluent concentration vs. time and indicates column utilization. At short times, adsorption happens upstream, and the effluent is free of the adsorbate. As time progresses, the adsorption front moves downstream, and the adsorbate is eventually breaking through the bed. Column regeneration occurs upon saturation. Figure 3 shows the single component breakthrough curves of each of the four species at different temperatures. Triplicate experiments are regressed using the statistical software Minitab to predict the 95% confidence interval. The breakthrough curves are fitted, as typically done, using the simple Thomas model (Eq. 15),[38,39] where k_{Thomas} is the adsorption rate constant [ml/(mg-min)], q_{Thomas} is the adsorbent loading of each component [g_{comp}/g_{ads}], t is the time [min], m_{ads} is the mass of the adsorbent [mg], and Q is the flowrate [mL/min]. The adsorption loading q_{Thomas}, estimated using the Thomas model, can also be obtained from the area between the curve and the $C/C_0 = 1$ line (C_0 is the entrance concentration).

$$\frac{C}{C_0} = \frac{1}{1 + \exp\left(-k_{Thomas}\, C_0 t + \frac{k_{Thomas} q_{Thomas} m_{ads}}{Q}\right)} \qquad (15)$$

A column packed with glass particles of similar diameter is used to estimate the residence time and dead space; its breakthrough curve is shown in Figure S7. This baseline loading is subtracted from the calculated q_{Thomas} value to acquire an accurate adsorption loading. The corrected q_{Thomas} values are shown in

Table 4, and these values match well with the batch q_{eq} at their respective equilibrium concentrations.

Like the batch experiments, the adsorption loading follows the HMF > LA> FA> fructose order. The higher the loading, the longer the time to breakthrough. As previously mentioned, the Thomas model assumptions are not valid in all cases; yet, the model still provides an acceptable fit and insights for comparison purposes.

Table 4: *Fitted parameters for data shown in Figure 3.* q_{Thomas} *has been baseline corrected and converted to the same units as in the batch isotherm for better comparison. Error bar corresponds to the 95% confidence interval of the triplicate experiments.*

Fitted Thomas parameters	**Temperature (K)**	**Adsorbate**			
		Fructose	**HMF**	**FA**	**LA**
k_{Thomas} (mL/mg-min)	298	0.390 ± 0.045	0.279 ± 0.013	1.160 ± 0.061	0.195 ± 0.024
	338	0.950	0.240	1.708	0.284
	363	1.752	0.365	3.208	0.662
q_{Thomas} ($mmol_i/g_{ads}$)	298	0.178 ± 0.009	3.158 ± 0.019	0.545 ± 0.003	1.821 ± 0.030
	338	0.113	2.331	0.313	1.388
	363	0.062	1.807	0.183	0.972
R^2	298	0.9869	0.9993	0.9981	0.9954
	338	0.9868	0.9965	0.9962	0.9817
	363	0.9851	0.9951	0.9892	0.9807

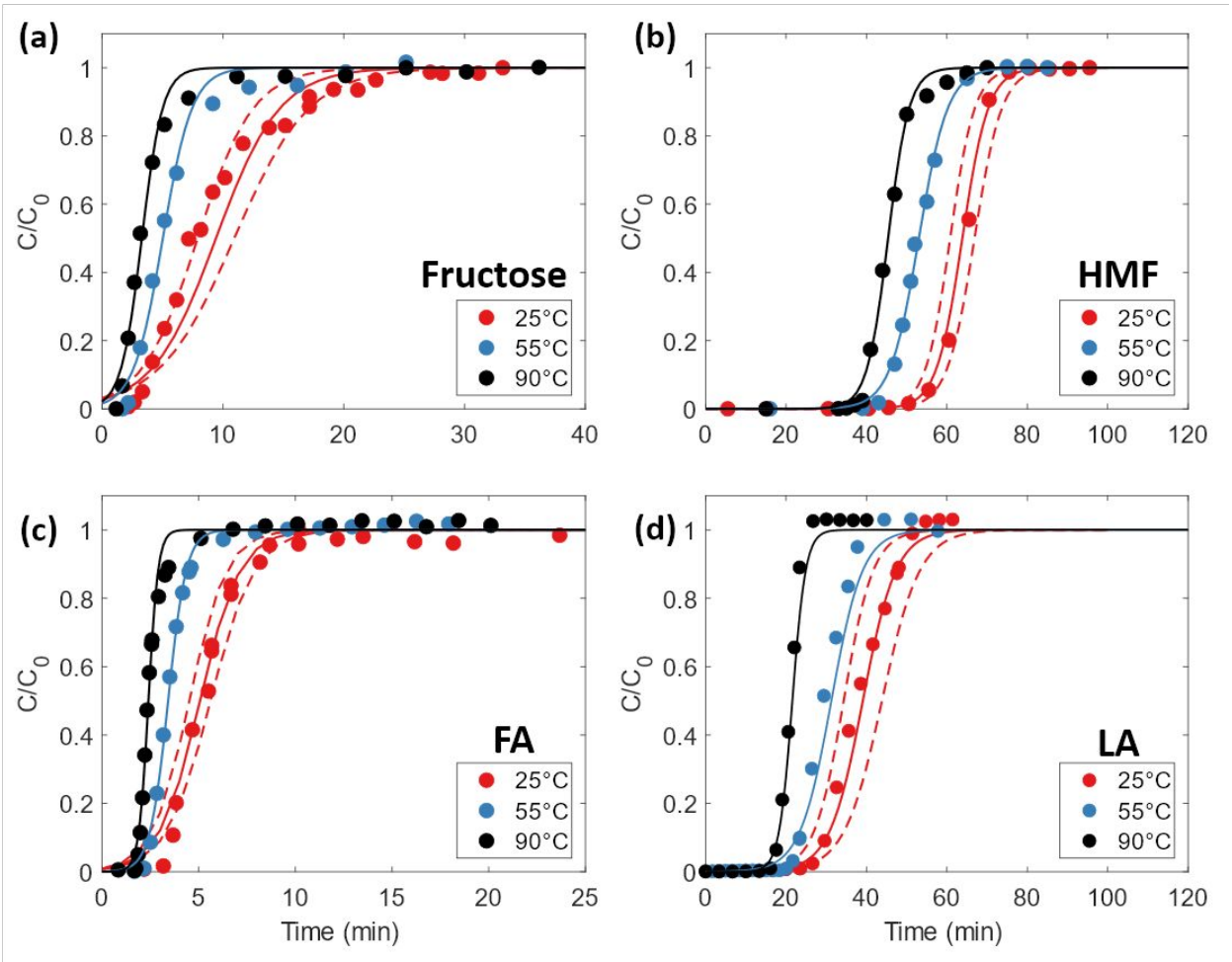

Figure 3: Continuous single component breakthrough curves for ***(a)*** *fructose,* ***(b)*** *HMF,* ***(c)*** *FA, and* ***(d)*** *LA. Points are quantified experimental values, and solid lines are curved fitted using the Thomas model. The fits are excellent. Dashed lines at 25 °C are 95% confidence intervals as an example of uncertainty.*

Similar to the aforementioned batch experiments, the adsorption selectivity in the continuous system was examined. Adsorption experiments of binary HMF-fructose solution and four-component of HMF, fructose, FA, and LA solution were conducted at 25 °C in hydrochloric acid potassium chloride buffer at pH = 0.7 (a typical catalyst of dehydration). No effect of the acid catalyst on adsorption is found. In the presence of fructose, the adsorption loading of HMF is only slightly lowered, as fructose adsorption is nearly negligible. On the other hand, HMF breakthrough happens faster (C/C_0 = 5% at t = 50 min), and the total amount of adsorbed HMF decreases when additional species, especially LA, are introduced. As evident in Figure 4b, LA is the biggest adsorption-site competitor for HMF with the second-highest adsorption capacity. All four components are first simultaneously adsorbed onto the bed. Still, as the bed approaches saturation, a roll-up of FA, LA, and fructose occurs, where these components are out-competed and replaced by HMF displaying regions with $C/C_0 > 1$. Even though FA's breakthrough occurs before fructose, more fructose desorbs during the roll-up, so that the adsorbed FA is still higher than fructose.

In these experiments, the adsorbate loading is determined by integrating the area above and below the curves. The separation factor of fructose, HMF, FA, and LA was calculated using Eq. 14 at t = 120 min, and the findings are similar to those shown in Figure 2b (0.02, 4.15, 0.09, and 0.10, respectively for the four components, despite the molar ratio of FA here being nearly triple

that of HMF, and LA having the same molar concentration as HMF). Thus, we can argue that the equilibrium of HMF dominates adsorption selectivity.

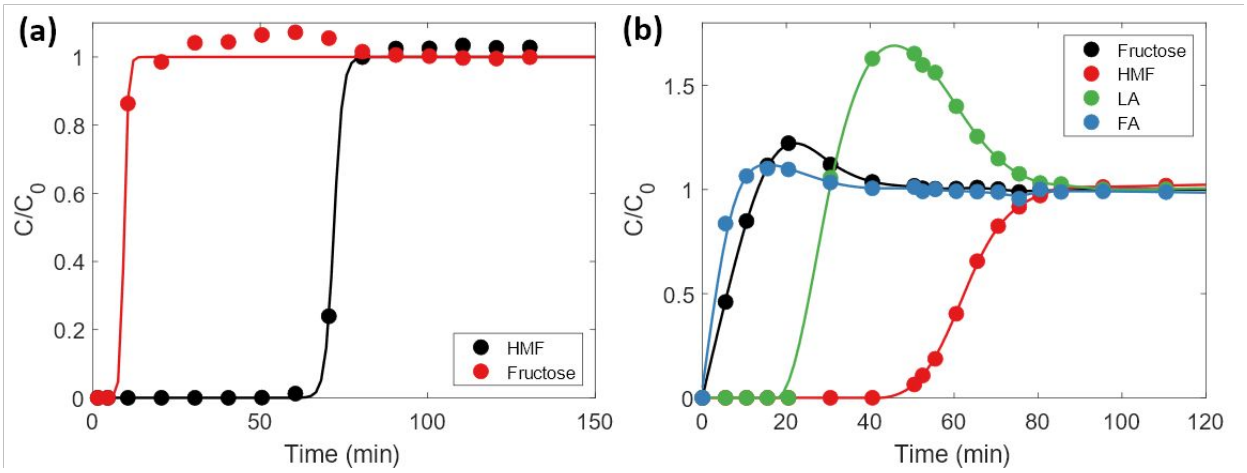

Figure 4: Breakthrough curves of multicomponent systems at room temperature. ***(a)*** *Binary adsorption of HMF and fructose in an equal-weight ratio (1.25 mg/mL), and* ***(b)*** *4-component adsorption of HMF, fructose, FA, and LA in an equal-weight ratio (1.25 mg/mL). A showcase of dynamic desorption (roll-up) of weakly adsorbed components by the preferentially adsorbing HMF.*

HMF Recovery by Solvent-induced Desorption

Rapid HMF recovery and purification are prerequisites for HMF process technology development. Solvent choice and desorption temperature were the two primary variables studied. The recovery data is shown in Figure 5 using both HPLC (points) and the online UV detector (lines) for water and IPA solvents. When the temperature is wrapped up from 25 °C to 90 °C, it takes about 8 min to reach the new temperature (Figure S8). Thus, even though the bed is isothermal spatially, a fraction of the experiments exhibits temporal temperature variation. This temperature variation makes the study of desorption kinetics non-trivial (something we do not pursue further here).

The elution curves exhibit an initial sharp increase followed by a gradual decrease. Water (the control solvent) is not as effective: in 45 min, only 32% of the adsorbed HMF is recovered at 25 °C due to its slight hydrophilicity. At 90 °C, the recovery increases to 59%, nearly double that at 25°C. Full recovery using water is unattainable (Figure 5b) at reasonable processing times.

Excitingly, IPA recovers >97% of HMF at 25 °C during 50 min of the experiment (Figure 5c) because HMF preferentially dissolves in the polar organic solvent. A high recovery is expected given previous overnight batch washings using alcohols.[27,28] By heating the IPA to 90 °C, full recovery HMF recovery is achieved in <25 min (Figure 5d). The overall percent recovery is overestimated (right vertical axis in Figure 5d) due to the sharp desorption peak at the beginning and the tail of the distribution. The full HMF recovery was independently confirmed due to having the same adsorption capacity in the next adsorption cycle over several cycles (see the section on the periodic process below).

IPA is a good solvent for desorption and can recover most of the HMF at room temperature. An increase in temperature decreases the processing time primarily. The low heat of adsorption implies that the temperature dependence is weak. The recovery productivity (amount recovered per unit time) is an essential metric for commercialization. The more than 2-fold recovery productivity enhancement from temperature swing desorption is excellent for process intensification. We propose that the heated desorption stream can be directed into a downstream

HMF process to reduce the associated reactor heat duty, e.g., in the hydrodeoxygenation reaction converting HMF into DMF.[55]

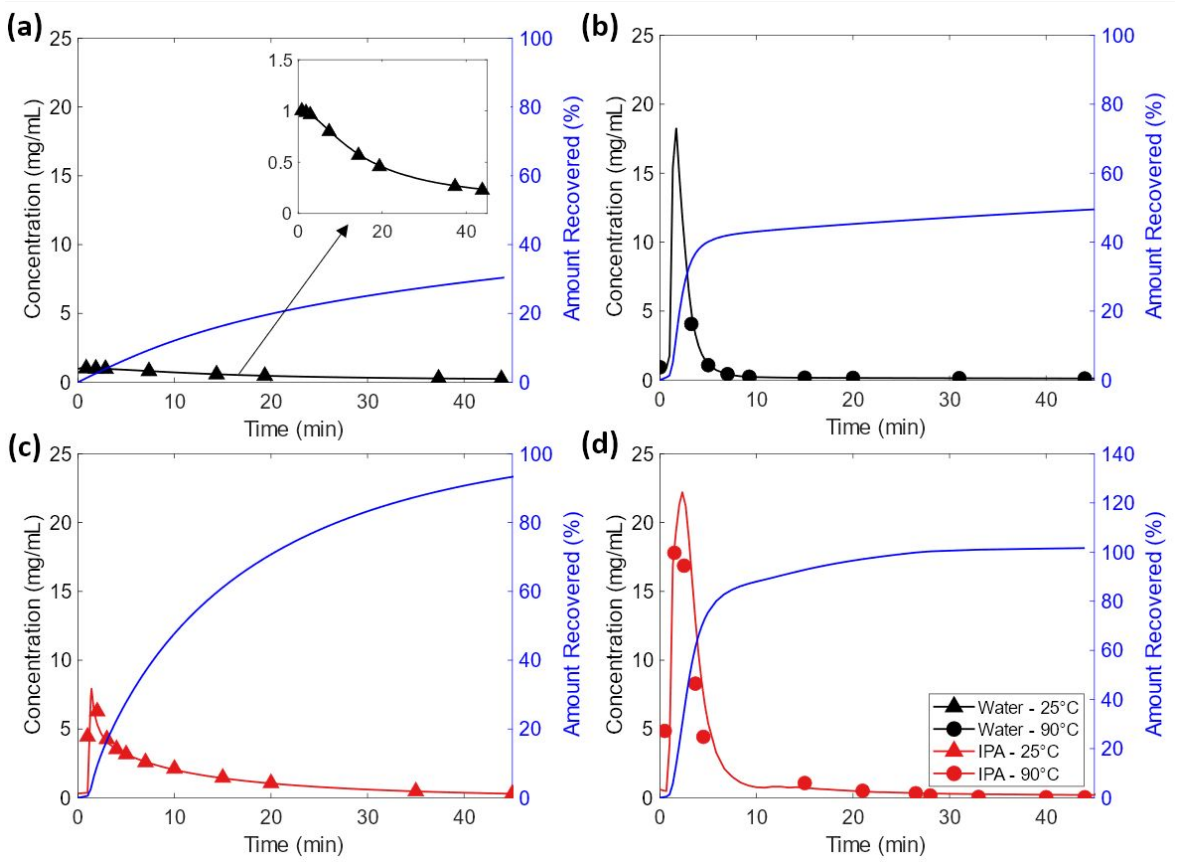

*Figure 5: Desorption of HMF from the column using water **(a & b)** or IPA **(c & d)** as the desorbing solvent at 25 ˚C **(a & c)** or 90 °C **(b & d)**. Time zero indicates the end of the adsorption cycle. The amount recovered was calculated using the cumulative amount desorbed divided by the amount adsorbed during an adsorption cycle. The red and black triangles and circles are averaged HPLC-quantified concentrations from collected samples over 30 s. The lines are from the absorbance of the in-line UV detector connected downstream of the column that gives continuous desorption curves due to the rapid time response. The HPLC quantified concentrations were used to calibrate the absorbance.*

Periodic Operation

Upon completing one cycle, the column was subjected to periodic operation. Figure S10 shows the breakthrough curves of the column upon multiple adsorption/desorption cycles. The near-identical breakthrough behavior suggests the full HMF recovery in each cycle. The system is robust – HMF recovery was carried out using different solvents and temperatures without performance deterioration. The low desorption temperature prevents HMF polymerization.

Simulation Predictions

The adsorption/desorption model with parameters obtained from batch experiments was solved. The *Pé* number is generally calculated from empirical correlations based on the particle diameter, *Re* number, and bed porosity. Given the values of Table 3, the *Pé* number calculated according to conventional correlations by Chung and Wen[60,72,73] and Gu et al.[73] should have been large (>>1), indicating a convection-dominated flow with negligible axial diffusion. However, *Pé* <1 shows good agreement with experimental HMF breakthrough data as a function of flowrate (Figure 6a). Calculations for single-component adsorption breakthrough curves of fructose, HMF, FA, and LA

on PBSAC at 25 °C (Figure 6b) also showed good fits to the experimental onset time with SSE of 2.97 x10^{-3}, 2.26 x10^{-2}, 1.77 x10^{-3}, and 1.94 x10^{-2}, respectively when the *Pé* values are small. The fitted *Pé* values are summarized in Tables S4 – S7. Therefore, we suspect that these correlations may be unsuited for microcolumns with more diffusive flux in the perpendicular direction of the flow – the experimental diameters for these correlations were generally much larger than the 2.36 mm column inner diameter used here. Correlations developed using smaller columns (column ID between 40-50 mm) have shown smaller *Pé* numbers (between 1-10) that are more similar in magnitude to our case.[74,75] A *Pé* correlation[65–67] incorporating the liquid hold-up volume[52,76] matches our system well. Liquid holdup applies when the fixed bed operates in the downflow direction as it was in this work. This method has been applied to systems using activated carbon adsorbents of 1 mm in diameter, and for $0.3 < Re_p < 3000$.[67] While this correlation was initially developed for trickled beds (gas-liquid-solid), Schwartz et al.[77] demonstrated that this *Pé* correlation is almost independent of the gas flow rate, making it applicable for standalone liquid adsorption systems at such conditions. The mentioned *Pé* comparison correlations are reproduced in the SI (Eq. S3 – S8).

The local equilibrium theory is deemed suitable for the desorption model with the good fit, but the *Pé* numbers leading to similar fits with the experimental data of HMF's desorption in IPA are 10-100x smaller, ranging between 0.04 (for 90 °C) and 0.15 (for 25 °C) (Figure 6c), in contrast to the *Pé* = 1.5 for HMF adsorption from water at 25 °C. While a value of *Pé* =1.46 is suitable for HMF desorption in water at 25 °C, smaller *Pé* values of ~0.03 describe the desorption of HMF in water at higher temperatures (Figure S11). The axial dispersion coefficient may change due to the solvent and temperature effects rendering the *Pé* correlation inaccurate. While not essential for this work, further understanding of transport correlations in microsystems would be welcome in the future.

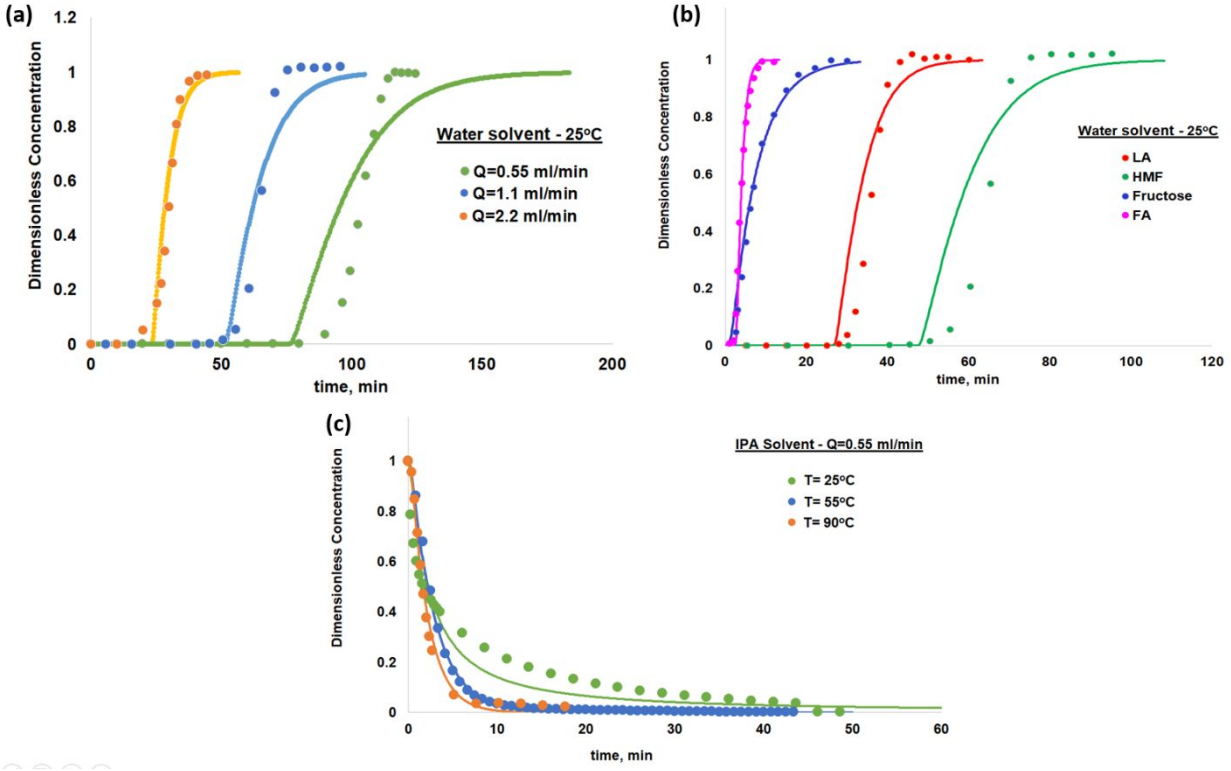

*Figure 6: Experimental (dots) and model predictions (lines) of **(a)** HMF breakthrough curves at different flow rates, **(b)** fructose, HMF, LA, and FA breakthrough curves at 25 °C and a flowrate of 1.1 mL/min, and **(c)** HMF desorption using IPA at 25, 55, and 90 °C.*

Operation under Realistic Feedstock Conditions

Adsorption at higher HMF concentrations (10 wt%) was performed in both batch and continuous systems to explore the practical use of the adsorption column. Single component isotherms are shown in Figure S12, and the HMF breakthrough curve in Figure S13. For competitive adsorption, synthetic fructose dehydration solutions were made with composition guided from the literature.[5,17] A maximum HMF yield is attained at 200 °C and 4 s reaction time, giving 93.1% fructose conversion and HMF, FA, and LA yields of 50.1, 17.7, and 7.9%, respectively. Experimental separation factors (α) were calculated and compared to predictions from the aforementioned IAST model. As shown in Figure 7a, the HMF separation factor drastically increases from 5.44 to ~14 when the FA and LA concentrations are lowered 10x to reflect realistic high HMF yield conditions. Similarly, the same roll-up effect was observed for the weakly adsorbed components in the continuous case (Figure 7b), and the α values are 0.03, 11.5, 0.02, and 0.04 for fructose, HMF, FA, and LA, respectively at t = 65 min. Again, the HMF α value is much higher here. The results under high yield concentrations highlight the applicability of an adsorption column for HMF separation under optimal fructose dehydration conditions. Alternative strategies, such as multi-stage adsorbers, can further boost HMF selectivity. Incorporating a different adsorbent (i.e., clay nano-adsorbent[78] or amberlite[79]) to specifically adsorb LA – the main competitive compound of HMF adsorption – is a possibility.

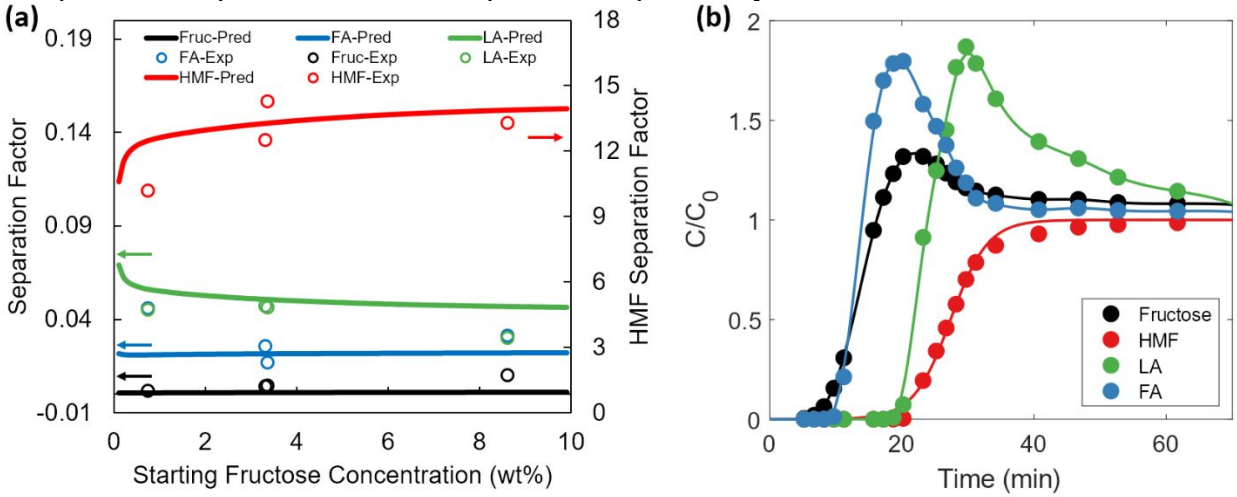

*Figure 7: Competitive adsorption of fructose, HMF, LA, and FA at realistic fructose dehydration conditions in **(a)** batch and **(b)** continuous systems. **(a)** Points are experimental data, and lines are the predictions from the IAST model with parameters from Table 2 and HMF isotherm parameters in Figure S12. Data show good agreement to IAST predictions. **(b)** Dynamic roll-up curves of the continuous adsorber. Experimental conditions: Temperature = 25 °C, flowrate = 0.2 mL/min, PBSAC weight = 375 mg. Inlet concentrations: fructose = 6.8 mg/mL, HMF = 30.2 mg/mL, LA = 5.1 mg/mL, and FA = 4.2 mg/mL.*

Comparative Cost and Energy Analysis

The purification and recovery of HMF from the fructose dehydration reaction has commonly been accomplished through traditional or vacuum distillation or by combining an extractor with flash tanks.[21] To assess the potential of the adsorption system and compare it to prior work, first, a

distillation model was built in Aspen Plus V11 using the NRTL-RK package to simulate a reference cost for HMF purification. Taken as an average value from the literature,[80–83] a saturated liquid stream of 10 wt% HMF in water (300 metric ton/day total flow rate) enters a 10-stage distillation column at 103 °C. A 99% purity for the HMF as the heavy key is a design specification. The equipment and utility costs are estimated using the built-in Aspen Process Economic Analyzer. Results are abridged and summarized in Figure 8 and Table S8, and further details are outlined in the SI.

A glaring issue is that the purified HMF stream exits at 200 °C (or 176 °C for 98% purity), temperatures at which HMF is known to self-polymerize into humins.[84,85] At reduced pressure (10 kPa), the boiling point decreases, and the bottom HMF stream exits at 109 °C with 98% purity from a vacuum distillation tower, alleviating partially the polymerization concerns. A 99% purity would increase the temperature to 137.5 °C. This high-temperature polymerization concern has not been brought up in the literature because prior techno-economic analyses have connected the product stream to a downstream hydrodeoxygenation reactor that turns HMF into DMF in the vapor phase.[81] A big hindrance of vacuum distillation is its equipment cost that is almost double that of a traditional distillation column. This is only partially offset by a 12% lower utility cost due to using medium pressure steam and a lower operating temperature.

The cost of HMF separation via adsorption is estimated by sizing an adsorption column to achieve the same productivity as a distillation column.[86] Two adsorption columns are needed to maintain continuous operation: one in the adsorption cycle and one in the regeneration (desorption) cycle. One could also explore increasing the number of cycles per day and using smaller beds. The cost estimates for various scenarios are detailed in the SI. The cost of two columns operating six cycles per day at 25 °C, processing a total of 30 ton/day of HMF, is \$88 k – this is less than $1/5^{th}$ of the distillation column and $1/10^{th}$ of the vacuum distillation (Figure 8). Furthermore, as shown in Figure 8 and Table S9, the adsorption bed energy use is only 9% of a vacuum distillation column. As utility cost often contributes ~10-20% to the process economics,[80,82,83] the demonstrated adsorption system herein presents an opportunity to reduce the minimal selling price (MSP) and the emitted carbon footprint. Thus, while raw material cost is a primary contributor to the MSP of HMF in general in biomass processing, and this also remains relevant here, the reduction in both capital and utility costs marks a promising opportunity. Finally, since IPA can be a downstream solvent,[55] this system can be easily integrated into DMF production over Ru/C catalyst with just one separation unit (a double column), achieving process intensification.

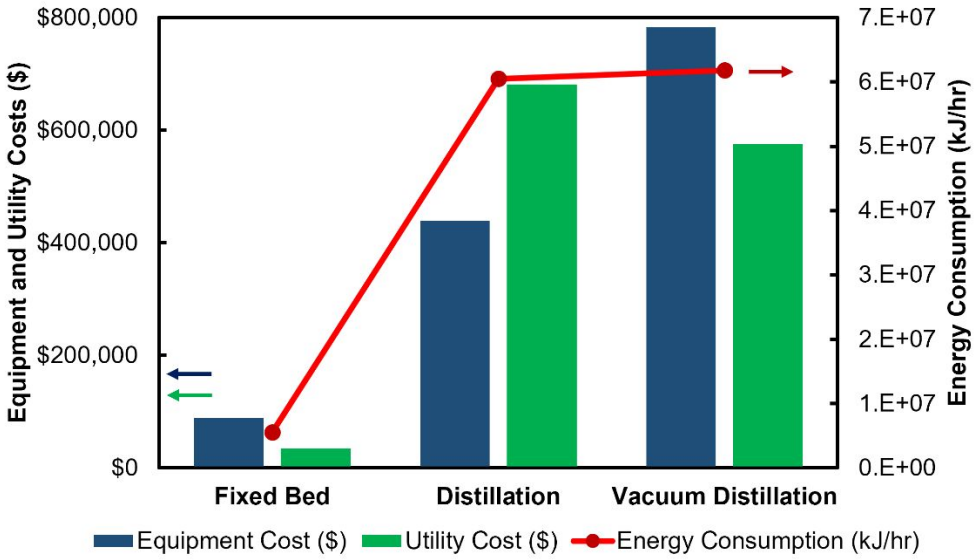

Figure 8: Cost and energy comparison of different separation methods. The energy consumption calculation only considered the heating and cooling portions of each scheme.

Conclusions

Biomass has emerged as a renewable and abundantly available carbon source for the production of chemicals and fuels to assist with decarbonization. Specifically, the conversion of biomass-derived saccharides to HMF using acid catalysts is attractive because HMF is a crucial platform chemical toward numerous value-added commodities. However, commercialization is hindered by the side reactions in the aqueous phase and HMF separation and purification.

We presented a temperature swing adsorption-desorption fixed-bed column using solid carbon adsorbent (PBSAC) to enable the purification of HMF from the aqueous stream and its transfer into a suitable solvent for downstream processing. We characterized the adsorption performance of PBSAC in both batch and continuous systems. PBSAC exhibits high capacity and separation factor for HMF due to its high surface area and low oxygen functionality. Multicomponent studies further pinpointed levulinic acid (LA) as the main competitor for HMF adsorption, while the hydrophilic fructose and formic acid (FA) are only weakly competitive. Selective adsorption of HMF appears to be slightly dependent on temperature.

Solvent choice and temperature are important for effective HMF desorption. Water is not an effective desorption solvent, as expected. In contrast, IPA is an excellent desorbing solvent. At 90 °C, full recovery of HMF from a saturated column can be achieved in <25 min. IPA has also been demonstrated by Jae *et al.*[55] to be a hydrogen donor and, in general, an excellent solvent for the hydrodeoxygenation of HMF into DMF over many catalysts.

We further analyzed the adsorption data using various isotherms to tabulate parameters for future use. We found that the Freundlich and Redlich-Peterson models gave comparable results and demonstrated that the IAST model is reasonable as a first pass model but needs improvement to become more quantitative. Furthermore, instead of using the Thomas model for breakthrough curves, due to supporting an analytical solution for ease of parameter estimation, and a different isotherm for the batch experiments, we proposed to numerically solve the governing equations using a consistent adsorption model between batch and flow experiments. We showcased an

adsorption and desorption model for the fixed bed that can be used for further scale-up and operational analyses and outlined challenges in terms of transport correlations in microfixed beds.

Importantly, seven complete cycles were demonstrated here without lack of performance, underscoring the promise for long-term operation. Excitingly, a simple techno-economic analysis highlights the favorable cost and energy expenditure compared to the traditional vacuum or regular distillation. The proposed approach effectively transfers HMF from the aqueous phase into an organic phase for downstream processing without producing a pure HMF stream.

Conflict of Interest

There are no conflicts of interest to declare.

Nomenclature

C	Concentration [M]
d_p	Particle diameter [m]
D_{ax}	Axial dispersion coefficient [m^2/s]
D_f	Diffusion coefficient [m^2/s]
g	Gravitational force [m/s^2]
k_{res}	Lumped mass transfer coefficient [s^{-1}]
	Equilibrium adsorption constant
K	Freundlich: [$(L/g_{carbon})^{1/n}$]
	Redlich-Peterson: [(L/g_{carbon})]
b_{RP}	Redlich-Peterson constant [$(L/mol)^n$]
n	Constant
m_{ads}	Adsorbent mass [mg]
Pé	Péclet number
Re	Reynold number
Sh	Sherwood number
Sc	Schmidt number
q	Adsorption loading [mol_i/g_{carbon}]
t	Time [min]
τ	Dimensionless time
v	Superficial Velocity [m/s]
V	Volume [ml]
W	Amount of HMF [mg]
z	Dimensionless length

Subscript / Superscript

eq	Equilibrium
i	Individual component
L	Langmuir
F	Freundlich
RP	Redlich-Peterson
$Thomas$	Thomas
a, d	Adsorbed, desorbed
exp	Experimental data

model	Model prediction
*	Dimensionless
Greek	
ε	Bed porosity/void fraction [-]
μ	Dynamic viscosity [kg/(m·s)]
ρ_{ads}	Adsorbent density [kg m^{-3}]

Acknowledgments
This work was supported by the Department of Energy's Office of Energy Efficient and Renewable Energy's Advanced Manufacturing Office under Award Number DE-EE0007888-8.3. The Delaware Energy Institute gratefully acknowledges the support and partnership of the State of Delaware toward the RAPID projects. The authors are grateful to Professor Abraham Lenhoff and Chase Herman for useful discussions on chromatography columns, Pierre Desir for valuable guidance on the construction of the micro-continuous process, Pavel Kots for the nitrogen adsorption-desorption isotherms, and Jiahua Zhou and Weiqing Zheng for the help with the XPS data collection and analysis.

References

1 R. A. Sheldon, M. Poliakoff, E. Perez, C. O. Tuck and I. T. Horvath, *Science (80-.).*, 2012, **337**, 695–699.
2 R. D. Perlack, L. L. Wright, A. F. Turhollow and R. L. Graham, *Biomass as Feedstock for Bioenergy*, 2005.
3 P. Gallezot, *Chem. Soc. Rev.*, 2012, 41, 1538–1558.
4 T. D. Swift, H. Nguyen, A. Anderko, V. Nikolakis and D. G. Vlachos, *Green Chem.*, 2015, **17**, 4725–4735.
5 T. D. Swift, C. Bagia, V. Choudhary, G. Peklaris, V. Nikolakis and D. G. Vlachos, *ACS Catal.*, 2014, **4**, 259–267.
6 Y. Roman-Leshkov and J. A. Dumesic, *Top. Catal.*, 2009, **52**, 297–303.
7 J. S. Kruger, V. Choudhary, V. Nikolakis and D. G. Vlachos, *ACS Catal.*, 2013, **3**, 1279–1291.
8 T. D. Swift, H. Nguyen, Z. Erdman, J. S. Kruger, V. Nikolakis and D. G. Vlachos, *J. Catal.*, 2016, **333**, 149–161.
9 S. Tschirner, E. Weingart, L. Teevs and U. Prüße, *Molecules*, 2018, **23**, 1866.
10 C. Lansalot-Matras and C. Moreau, *Catal. Commun.*, 2003, **4**, 517–520.
11 Y. Roman-Leshkov, J. N. Chheda and J. A. Dumesic, *Science (80-.).*, 2006, **312**, 1933–1937.
12 R. M. Musau and R. M. Munavu, *The Preparation of 5-Hydroxymethyi-2-Furaldehyde (HMF) from D-Fructose in the Presence of DMSO*, 1987, vol. 13.
13 H. Zhao, J. E. Holladay, H. Brown and Z. C. Zhang, *Science (80-.).*, 2007, **316**, 1597–1600.
14 S. Eminov, J. D. E. T. Wilton-Ely and J. P. Hallett, *ACS Sustain. Chem. Eng.*, 2014, **2**, 978–981.
15 T. Shimanouchi, Y. Kataoka, T. Tanifuji, Y. Kimura, S. Fujioka and K. Terasaka, *AIChE J.*, 2016, **62**, 2135–2143.
16 E. Weingart, S. Tschirner, L. Teevs and U. Prüße, *Molecules*, 2018, **23**, 1802.
17 P. Desir, B. Saha and D. G. Vlachos, *Energy Environ. Sci.*, 2019, **12**, 2463–2475.
18 J. Lueckgen, L. Vanoye, R. Philippe, M. Eternot, P. Fongarland, C. de Bellefon and A.

Favre-Réguillon, *J. Flow Chem.*, 2018, **8**, 3–9.
19 S. Mohammad, C. Held, E. Altuntepe, T. Köse and G. Sadowski, *J. Phys. Chem. B*, 2016, **120**, 3797–3808.
20 Y. Muranaka, H. Nakagawa, R. Masaki, T. Maki and K. Mae, *Ind. Eng. Chem. Res.*, 2017, **56**, 10998–11005.
21 D. W. Brown, A. J. Floyd, R. G. Kinsman and Y. Roshan-Ali, *J. Chem. Technol. Biotechnol.*, 1982, **32**, 920–924.
22 A. C. Ijzer, E. Vriezekolk, T. Dekic Zivkovic and K. Nijmeijer, *J. Chem. Technol. Biotechnol.*, 2016, **91**, 96–104.
23 R. Ranjan, S. Thust, C. E. Gounaris, M. Woo, C. A. Floudas, M. von Keitz, K. J. Valentas, J. Wei and M. Tsapatsis, *Microporous Mesoporous Mater.*, 2009, **122**, 143–148.
24 P. Vinke and H. van Bekkum, *Starch - Stärke*, 1992, **44**, 90–96.
25 W. C. Yoo, N. Rajabbeigi, E. E. Mallon, M. Tsapatsis and M. A. Snyder, *Microporous Mesoporous Mater.*, 2014, **184**, 72–82.
26 H. Ma, *J. Energy Nat. Resour.*, 2017, **6**, 24.
27 T. D. Swift, C. Bagia, V. Nikolakis, D. G. Vlachos, G. Peklaris, P. Dornath and W. Fan, *AIChE J.*, 2013, **59**, 3378–3390.
28 C. Detoni, C. H. Gierlich, M. Rose and R. Palkovits, *ACS Sustain. Chem. Eng.*, 2014, **2**, 2407–2415.
29 Y. B. Zhang, Q. X. Luo, M. H. Lu, D. Luo, Z. W. Liu and Z. T. Liu, *Chem. Eng. J.*, 2019, **358**, 467–479.
30 J. Zheng, X. He, C. Cai, J. Xiao, Y. Liu, Z. Chen, B. Pan and X. Lin, *Chemosphere*, 2020, **239**, 124732.
31 M. Yabushita, P. Li, H. Kobayashi, A. Fukuoka, O. K. Farha and A. Katz, *Chem. Commun.*, 2016, **52**, 11791–11794.
32 R. C. Kuhn, M. A. Mazutti and F. M. Filho, *LWT - Food Sci. Technol.*, 2012, **48**, 127–133.
33 R. Xiong, M. León, V. Nikolakis, S. I. Sandler and D. G. Vlachos, *ChemSusChem*, 2014, **7**, 236–244.
34 H. Jin, Y. Li, X. Liu, Y. Ban, Y. Peng, W. Jiao and W. Yang, *Chem. Eng. Sci.*, 2015, **124**, 170–178.
35 P. Dornath and W. Fan, *Microporous Mesoporous Mater.*, 2014, **191**, 10–17.
36 B. Böhringer, O. Guerra Gonzalez, I. Eckle, M. Müller, J. M. Giebelhausen, C. Schrage and S. Fichtner, *Chemie-Ingenieur-Technik*, 2011, **83**, 53–60.
37 M. A. Al-Ghouti and D. A. Da'ana, *J. Hazard. Mater.*, 2020, **393**, 122383.
38 H. C. Thomas, *Ann. N. Y. Acad. Sci.*, 1948, **49**, 161–182.
39 Z. Xu, J. Cai and B. Pan, *J. Zhejiang Univ. Sci. A*, 2013, **14**, 155–176.
40 J. R. Rao and T. Viraraghavan, *Bioresour. Technol.*, 2002, **85**, 165–171.
41 P. Muthamilselvi, R. Karthikeyan, A. Kapoor and S. Prabhakar, *Int. J. Ind. Chem.*, 2018, **9**, 379–390.
42 D. C. K. Ko, V. K. C. Lee, J. F. Porter and G. Mckay, *J. Chem. Technol. Biotechnol.*, 2002, **77**, 1289–1295.
43 V. Manirethan and R. M. Balakrishnan, *Environ. Technol. Innov.*, 2020, **20**, 24723–24737.
44 J. Jae, W. Zheng, A. M. Karim, W. Guo, R. F. Lobo and D. G. Vlachos, *ChemCatChem*, 2014, **6**, 848–856.
45 P. Panagiotopoulou, N. Martin and D. G. Vlachos, *ChemSusChem*, 2015, **8**, 2046–2054.
46 N. Rajabbeigi, R. Ranjan and M. Tsapatsis, *Microporous Mesoporous Mater.*, 2012, **158**,

253–256.
47 M. H. Kim, C. S. Kim, H. W. Lee and K. Kim, *J. Chem. Soc. - Faraday Trans.*, 1996, **92**, 4951–4956.
48 N. Akiya and P. E. Savage, *AIChE J.*, 1998, **44**, 405–415.
49 B. J. Liu, Z. J. Hu and Q. L. Ren, *Colloids Surfaces A Physicochem. Eng. Asp.*, 2009, **339**, 185–191.
50 M. León, T. D. Swift, V. Nikolakis and D. G. Vlachos, *Langmuir*, 2013, **29**, 6597–6605.
51 GE Healthcare, *Appl. note 28-9372-07 AA*, 2010, 1–6.
52 K. Miyabe and G. Guiochon, *J. Chromatogr. A*, 1999, **830**, 29–39.
53 K. Miyabe and G. Guiochon, *J. Chromatogr. A*, 1999, **857**, 69–87.
54 A. S. Rathore, R. M. Kennedy, J. K. O'Donnell, I. Bemberis and O. Kaltenbrunner, *BioPharm Int.*, 2003, 16, 30–40.
55 J. Jae, W. Zheng, R. F. Lobo and D. G. Vlachos, *ChemSusChem*, 2013, **6**, 1158–1162.
56 D. M. LeVan, G. Carta and C. M. Yon, in *Perry's Chemical Engineers' Handbook*, McGrawHill, New York, 7th edn., 1997.
57 M. S. Shafeeyan, W. M. A. Wan Daud and A. Shamiri, *Chem. Eng. Res. Des.*, 2014, 92, 961–988.
58 S. Brandani, *Adsorption*, 2020, **1**, 3.
59 R. Perry, D. Green and J. Maloney, *Perry's Chemical Engineers' Handbook*, McGrawHill, New York, 1997.
60 F. Grote, I. Ermilova and A. P. Lyubartsev, *J. Phys. Chem. B*, 2018, **122**, 8416–8428.
61 L. A. Dunn and R. H. Stokes, *Aust. J. Chem*, 1965, **18**, 285–296.
62 A. C. F. Ribeiro, O. Ortona, S. M. N. Simões, C. I. A. V. Santos, P. M. R. A. Prazeres, A. J. M. Valente, V. M. M. Lobo and H. D. Burrows, *J. Chem. Eng. Data*, 2006, **51**, 1836–1840.
63 J. F. Gabitto and N. O. Lemcoff, *Chem. Eng. J.*, 1987, **35**, 69–74.
64 G. Pigorini and M. D. LeVan, *Ind. Eng. Chem. Res.*, 1999, **38**, 2439–2449.
65 V. Specchia and G. Baldi, *Chem. Eng. Sci.*, 1977, **32**, 515–523.
66 A. J. Colombo, G. Baldi and S. Sicardi, *Chem. Eng. Sci.*, 1976, **31**, 1101–1108.
67 V. J. Inglezakis and S. G. Poulopoulos, *Adsorption, Ion Exchange and Catalysis*, Elsevier, 2006.
68 R. Blume, D. Rosenthal, J. P. Tessonnier, H. Li, A. Knop-Gericke and R. Schlögl, *ChemCatChem*, 2015, **7**, 2871–2881.
69 D. Weingarth, R. Drumm, A. Foelske-Schmitz, R. Kötz and V. Presser, *Phys. Chem. Chem. Phys.*, 2014, **16**, 21219–21224.
70 T. Chen, Y. Chen and P. Bai, *Ind. Eng. Chem. Res.*, 2020, **59**, 8323–8334.
71 J. Zhang and E. Weitz, *ACS Catal.*, 2012, **2**, 1211–1218.
72 M. Suzuki and J. M. Smith, *Chem. Eng. J.*, 1972, **3**, 256–264.
73 S. Omid Rastegar and T. Gu, *J. Chromatogr. A*, 2017, **1490**, 133–137.
74 K. N. Son, J. A. Weibel, S. V Garimella and J. C. Knox, *Calibration and Sensitivity of a Fixed-Bed Adsorption Model for Atmosphere Revitalization in Space*, 2017.
75 J. Kim, G. Hart and C. Yi, *Axial Dispersion of Gas in a Circulating Fluidized Bed*, 2002, vol. 19.
76 K. Miyabe and A. Okada, *Analyst*, 2002, **127**, 1420–1426.
77 J. G. Schwartz, E. Weger and M. P. Duduković, *AIChE J.*, 1976, **22**, 953–956.
78 N. Baylan, *Biomass Convers. Biorefinery*, 2020, **10**, 1291–1300.

79 D. Datta and H. Uslu, *J. Mol. Liq.*, 2017, **234**, 330–334.
80 F. K. Kazi, A. D. Patel, J. C. Serrano-Ruiz, J. A. Dumesic and R. P. Anex, *Chem. Eng. J.*, 2011, **169**, 329–338.
81 Y. Román-Leshkov, C. J. Barrett, Z. Y. Liu and J. A. Dumesic, *Nature*, 2007, **447**, 982–985.
82 Z. Lin, V. Nikolakis and M. Ierapetritou, *Ind. Eng. Chem. Res.*, 2014, **53**, 10688–10699.
83 A. H. Motagamwala, K. Huang, C. T. Maravelias and J. A. Dumesic, *Energy Environ. Sci.*, 2019, **12**, 2212–2222.
84 B. F. M. Kuster, *Starch - Stärke*, 1990, **42**, 314–321.
85 I. K. M. Yu and D. C. W. Tsang, *Bioresour. Technol.*, 2017, **238**, 716–732.
86 G. Towler and R. Sinnott, in *Chemical Engineering Design: Principles, Practice and Economics of Plant and Process Design*, Butterworth-Heinemann, Elsevier Ltd., Waltham, MA, 2nd edn., 2013.